Materials Advances

ROYAL SOCIETY OF CHEMISTRY

PAPER

View Article Online
View Journal | View Issue

Check for updates

Cite this: *Mater. Adv.*, 2025, 6, 9133

Preparation of a Ti–Al–Si based intermetallic alloy from Ti6Al4V and AlSi10Mg powders by laser powder bed fusion and hot isostatic pressing

Tomas Cegan,[a] Jan Jurica,[a] Katerina Skotnicova,[a]* Marek Pagac,[b] Michaela Stamborska,[c] Lukas Horsak,[a] Jiri Hajnys,[b] Jakub Mesicek[b] and Konda Gokuldoss Prashanth[de]

Received 14th February 2025,
Accepted 11th October 2025

DOI: 10.1039/d5ma00139k

rsc.li/materials-advances

A Ti–44Al–1.7V–0.2Mg–4.5Si (at%) alloy was successfully fabricated *via* laser powder bed fusion (LPBF) using a blend of Ti6Al4V and AlSi10Mg powders. Optimized process parameters, including low laser power (80–100 W), a hatch spacing of ~0.12 mm, and high scan speeds (~1400 mm s^{-1}), were critical for achieving the desired dimensions and quality. Despite optimization, the microstructure revealed defects such as cracks, pores, and unmelted Ti-based particles. Subsequent hot isostatic pressing (HIP) reduced these defects by up to 90% and improved microstructural homogeneity by eliminating unmelted particles. Heat treatment (HT) further refined the structure, producing a multiphase composition dominated by γ-TiAl, α_2-Ti_3Al and Ti_5Si_3 precipitates. Mechanical testing revealed anisotropic behaviour, with hardness, compressive yield strength, and plastic deformation at room temperature (RT) higher in the direction perpendicular to the build direction. The alloy demonstrated excellent high-temperature resistance, achieving a maximum compressive strength of ~1000 MPa at RT, 490 MPa at 850 °C, and 350 MPa at 900 °C. This study presents a novel LPBF-based method for fabricating TiAl-based alloys, combining HIP and HT to enhance microstructural quality and mechanical performance, paving the way for advanced high-temperature applications.

Open Access Article. Published on 28 October 2025. Downloaded on 6/20/2026 5:31:48 PM.
This article is licensed under a Creative Commons Attribution 3.0 Unported Licence.

1. Introduction

For more than two decades, TiAl-based alloys have been considered as very promising materials (in aerospace, automotive, energy industries, *etc.*) due to their combination of low density and excellent high-temperature resistance (specific high-temperature strength).[1–3] Of the many investigated TiAl-based alloys, the technically important alloys (due to good creep resistance) showed fully or nearly lamellar microstructures when alloyed with refractory metals Nb, Ta, W, and Mo (<8 at%) or when precipitation-hardened by Si and C (<1 at%) or when using a combination of these mentioned alloying elements.[4–9] These alloys were usually prepared using conventional metallurgical techniques like arc melting, vacuum induction melting, *etc.* However, the high reactivity of the TiAl melt limits the choice of crucibles (limited to Y_2O_3, $BaZrO_3$, water-cooled copper, or isostatically pressed graphite).[10–13] In addition, the casting conditions must be precisely controlled to avoid contamination and Al loss.[12,13] Cast TiAl alloys contain a typical coarse-grained columnar microstructure, which is usually refined using hot isostatic pressing (HIP) or by appropriate heat treatment (HT).[14,15] HIP is often recommended to eliminate casting defects.[16,17] Pre-alloyed atomized powders were generally used to prepare TiAl products through powder metallurgy (PM).[18,19] However, to obtain a high-quality atomized powder, appropriate input ingots without impurities and with a homogeneous composition are necessary and are restricted by the cost and limited availability of feedstock. For cast and PM TiAl products, another factor limiting their application is fragility at RT (room temperature) and associated low machinability.[1,20]

Additive manufacturing (AM) offers the advantage of fabricating near-net-shape and complex-shaped products with high dimensional accuracy.[21–24] Hence, AM is a very promising

[a] *VSB – Technical University of Ostrava, Faculty of Materials Science and Technology, 70800 Ostrava, Czech Republic. E-mail: katerina.skotnicova@vsb.cz; Tel: +420596993404*
[b] *VSB – Technical University of Ostrava, Faculty of Mechanical Engineering, 70800 Ostrava, Czech Republic*
[c] *Institute of Materials and Machine Mechanics, Slovak Academy of Sciences, Dubravska Cesta 9, 845 13 Bratislava, Slovak Republic*
[d] *Department of Mechanical and Industrial Engineering, Tallinn University of Technology, Ehitajate tee 5, 19086 Tallinn, Estonia*
[e] *Centre for Biomaterials, Cellular and Molecular Theranostics (CBCMT), Vellore Institute of Technology, School of Mechanical Engineering, Vellore, Tamil Nadu, 632014, India*

© 2025 The Author(s). Published by the Royal Society of Chemistry

Open Access Article. Published on 28 October 2025. Downloaded on 6/20/2026 5:31:48 PM. This article is licensed under a Creative Commons Attribution 3.0 Unported Licence.

technology to produce TiAl complex parts. Due to the feedstock availability, most of the reports related to the fabrication of AM TiAl-based alloys are limited to the Ti–48Al–2Cr–2Nb alloy.[25–27] Currently, laser powder bed fusion (LPBF), electron beam powder bed fusion (EPBF), and laser melting deposition (LMD) are employed to fabricate TiAl alloy parts.[25–30] While EPBF can fabricate crack-free TiAl due to powder-bed heating to 1000 °C, the LPBF process leads to cracking and these cracks cannot be eliminated by adjusting the LPBF process parameters.[26–31] The cracking may be attributed to the extreme cooling conditions inducing thermal stresses during solidification.[32,33] The cracks may be eliminated by changing the chemical composition or adding a grain refiner in the form of fine dispersion particles.[26–29] Dzogbewu[31] suggests the reduction of the temperature gradient between individual layers by heating the entire build chamber to avoid cracking during the fabrication of TiAl by the LPBF process. HIP technology may be employed for crack elimination by closure which may be due to the combination of diffusion, plastic deformation, and compression creep. Only a limited number of studies have investigated the HIP process for LPBF TiAl, particularly with respect to crack elimination.

Currently, LPBF focuses primarily on melting pre-alloyed powders into a final product.[25–27] However, this study opens a new dimension, where a combination of two different compositions is employed to achieve a third composition by *in situ* alloying. Commercially available and the most used Ti6Al4V and AlSi10Mg powders (relatively inexpensive than TiAl powders) were used as the feedstock materials. Similar research was carried out by Dilip *et al.*,[34] where a mixture of atomized Ti–6Al–4V and Al powders was used to fabricate 3D TiAl parts by binder jetting and reactive sintering. Polozov *et al.*[35] and Nepapushev *et al.*[36] fabricated parts based on Ti_2AlNb and $TiAl_2$, respectively, using elemental powders by LPBF. Although these attempts faced issues related to compositional heterogeneity and formation of porosity, *in situ* alloying offers important benefits: reduced reliance on expensive pre-alloyed powders, potential for flexible composition design, and alignment with sustainability goals by minimizing waste and energy consumption.

Recent work by Kim *et al.*[37] demonstrated that *in situ* alloying of a nonequiatomic TiNbMoTaW refractory high-entropy alloy (HEA) by LPBF is feasible, provided the elemental ratios are carefully designed to minimize the liquidus–solidus interval. These studies revealed that micro-segregation can be suppressed. However, achieving chemical homogeneity, appropriate microstructure and mechanical properties in multi-element systems remains a significant challenge. These insights are highly relevant, as they underscore the importance of melt behaviour and phase stability when applying *in situ* alloying to more sensitive binary systems such as TiAl. Indeed, in TiAl systems, the sharp phase boundaries, reactivity of Ti and Al, and high propensity for oxide or intermetallic formation introduce additional complexity.

Hence, this study aimed to assess the possibility of fabricating an intermetallic TiAl-based Ti–44Al–1.7V–0.2Mg–4.5Si (at%) alloy by the combination of LPBF and HIP processes. The addition of Si improves the oxidation and creep resistance in TiAl due to the formation of an oxide layer and by precipitation of the Ti_5Si_3 phase.[38,39] The influence of Mg addition was studied by Sun *et al.*,[40] where an addition of 0.5 at% Mg was found to lead to the formation of Mg-rich phases in the Ti–48Al binary alloy increasing their mechanical properties. Wang *et al.*[41] studied the effect of 2 at% V on the creep resistance of the Ti–44Al–6Nb–1Cr alloy at 800 °C. Knaislová *et al.*[8,38,39] studied the fabrication of Ti–(10–20)Al–(15–30)Si (at%) alloys by both casting and powder metallurgical (mechanical alloying combined with spark plasma sintering) routes. It was observed that the Ti–(10–20)Al–(15–30)Si (at%) alloys show high hardness and excellent wear resistance (comparable to tool steels) but are significantly brittle regardless of the fabrication technique. The crack initiates around Ti_5Si_3 silicide; hence, a lower Si content was chosen for the present study. Moreover, it was assumed that the LPBF process enables the formation of fine and evenly distributed Ti_5Si_3 precipitates in the TiAl matrix, which can significantly reduce brittleness (compared to TiAl with large-size silicides).

It is emphasized that the present study is the first of its kind to fabricate Ti–44Al–1.7V–0.2Mg–4.5Si (at%) alloys. In addition, TiAl-based alloys with the combination of V, Si, and Mg have not yet been attempted by LPBF. The present study aims to address the following: (1) can LPBF fabricate TiAl-based alloys with desired geometry from the Ti6Al4V and AlSi10Mg powder mixtures? (2) In the first instance, can external defects like cracks and porosity can be avoided? If not, can they be eliminated by HIP post-processing? (3) Can a homogeneous microstructure consisting of TiAl, Ti_3Al phase, and fine-strengthening Ti_5Si_3 particles be prepared using LPBF? Or do the HIP and/or heat treatment (HT) methods lead to the formation of such a homogeneous microstructure? (4) Can improved mechanical properties, including high-temperature properties, be achieved in such kind of alloys?

2. Materials and methods

2.1. Starting powder and printing conditions

Ti6Al4V ELI and AlSi10Mg powders from Trumpf were used for the present study. Both types of powders were not virgin and had been used ten times before building the LPBF 3D parts. The large and sintered particles were separated out by sieving the powder through a sieve with a mesh size of 63 μm. Subsequently, the powders were mixed in a ratio of 2.3 : 1 (wt%) using a 3D powder blender mixer Turbula type T2F for 15 min. A Trumpf Truprint 1000 machine was used for the fabrication where 15 TiAl-based rods with a diameter of 13 mm and a length of 85 mm were fabricated. An unheated Ti substrate was used in an Ar atmosphere with a purity of 5.0 (99.998%) for the fabrication of these samples. Table 1 furnishes the parameters and hatch style employed for the LPBF process. The print preview, laser trajectories, and image of samples after LPBF are presented in Fig. 1 and 2.

2.2. Hot isostatic pressing (HIP)

The samples after LPBF were subjected to the HIP process: 6 samples were processed at a temperature of 1200 °C and

 © 2025 The Author(s). Published by the Royal Society of Chemistry

Open Access Article. Published on 28 October 2025. Downloaded on 6/20/2026 5:31:48 PM. This article is licensed under a Creative Commons Attribution 3.0 Unported Licence.

Table 1 Process parameters employed to fabricate the Ti–Al samples using the LPBF process

Parameter	Value
Layer thickness – slicing	20 μm
Focus size (spot size)	55 μm
Print strategies	Meander, chessboard
Hatch offset	0.08 mm
Hatch distance	0.12 mm
Laser speed (hatch)	1400 mm s^{-1}
Laser power (hatch)	80 W, 100 W
Laser speed (contour)	2000 mm s^{-1}
Laser power (contour)	80 W, 100 W

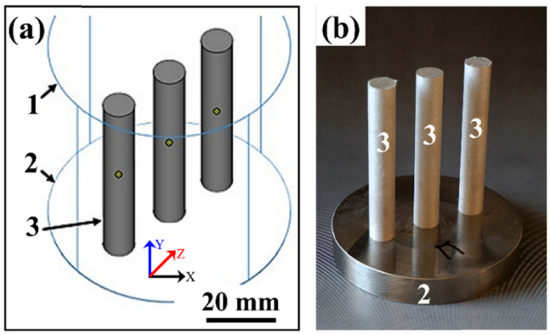

Fig. 1 (a) The 3D print preview of samples in Materialise Magics software and (b) image of samples after 3D printing: (1) bounding box of the Trumpf TruPrint 1000 3D printer build area (blue lines), (2) substrate, and (3) vertical samples.

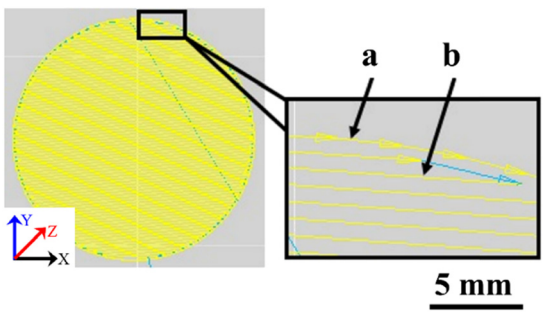

Fig. 2 Schematics showing the details of the meander hatching strategy employed during the fabrication of the Ti–Al samples in the TruTops Print Viewer slicer. (a) The laser trajectory used at the contours and (b) the laser trajectory for the hatches.

a pressure of 150 MPa with a dwell time of 2 h (HIP_1 process); the other 6 samples were processed under the same pressure and time, but at a higher temperature of 1240 °C (HIP_2 process). An EPSI hot isostatic press was used, with a heating rate of 10 °C min^{-1}, and subjected to furnace cooling. Individual samples were vertically placed in a corundum crucible, during the HIP process. Before heating and applying pressure, the HIP chamber was purged with Ar with purity 5.0 (3×) and evacuated to 100 Pa for 10 min. The temperature and pressure records from the HIP processes are shown in Fig. 3.

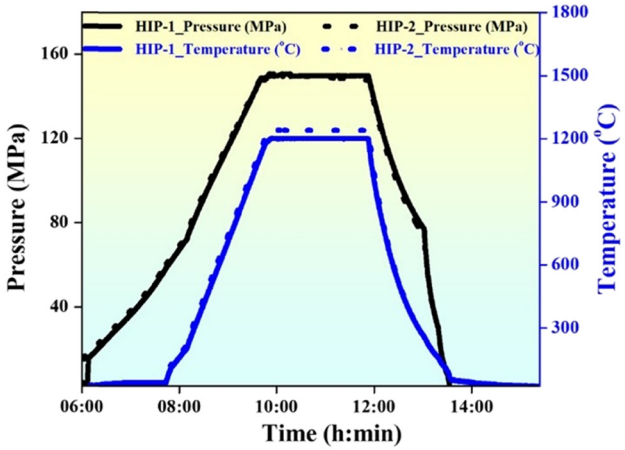

Fig. 3 Temperature and pressure distribution profile for the Ti–Al samples processed using the hot isostatic pressing (HIP) process.

The selection of temperatures for HIP is based on the two-phase (α + γ) region of the binary Ti–Al diagram. They are frequently applied during HIP of cast Ti–Al alloys due to good plasticity of TiAl based materials at these temperatures.[4,7,9]

2.3. Heat treatment (HT)

The samples were heat treated at 1370 °C for 20 min in a XERION XVAC furnace. The HT temperature is based on the single-phase α region in the binary Ti–Al diagram.[4,7] The HT process takes place under a dynamic Ar (5.0) atmosphere with a flow rate of 2 L min^{-1}. A heating rate of 10 °C min^{-1} was used and the samples were furnace cooled. The temperature regulation was carried out using a thermocouple placed near the processed samples. Before heating, the furnace chamber was evacuated to a pressure of 0.15 Pa for 5 min and the temperature profile is shown in Fig. 4.

2.4. Microstructural and chemical analysis

The samples for metallographic investigation were cut using an electro-erosion cutting (EDM) CHMER machine. The microstructure of the samples was characterized in both transverse and longitudinal directions. Standard metallographic techniques were employed for sample preparation: moulding into electrically conductive resin, grinding on wet sandpaper (grit 200 to 2000 (grains per cm^2)), and polishing with Al_2O_3 suspension (particle size from 1 to 0.3 μm). Both an optical microscope (OM; Olympus GX 51) and a scanning electron microscope (SEM; Quanta 450 FEG) equipped with an energy-dispersive X-ray spectrometer (EDS) were used for microstructure characterization. All metallographic observations (OM and SEM/BSE) were performed on sections cut in either the XY-plane (transverse cut to the build direction) or the XZ-plane (longitudinal to the build direction). The presence of porosity, defects, and individual phases was determined using the ImageJ software with automated images. A minimum of 10 images were recorded for each sample being subjected to automated image analysis by ImageJ. The O, H, and N elemental analysis was performed by using a LECO ONH 836

Open Access Article. Published on 28 October 2025. Downloaded on 6/20/2026 5:31:48 PM. This article is licensed under a Creative Commons Attribution 3.0 Unported Licence.

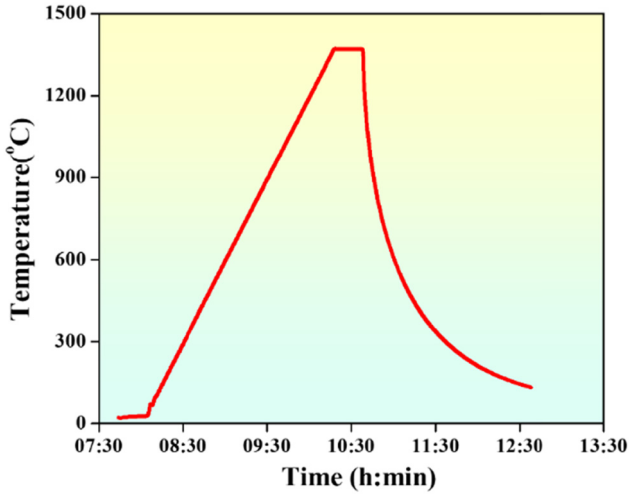

Fig. 4 Temperature profile observed for the LPBF Ti–Al samples during the heat treatment process.

elemental analyser based on the combustion method using graphite crucibles.

2.5. Phase identification and density measurement

The X-ray diffraction (XRD) analysis was carried out using a Bruker D8 DISCOVER diffractometer equipped with an X-ray tube with a rotating Cu anode operating at 12 kW. All measurements were performed in parallel beam geometry with a parabolic Goebel mirror in the primary beam. The diffraction patterns were measured within an angular range (2θ) of 20°–90° with an exposure time of 5 s and a step size of 0.05°. The AccuPyc II 1340 He gas pycnometer with an integrated analysis module was used for measuring the skeletal density. The resulting density was determined based on 10 cycles for each measured sample.

2.6. Hardness and compression test

The mechanical behaviour of LPBF Ti–Al-based samples was measured by hardness and compressive tests. The hardness measurement was performed on a Qness A+ Evo device at a load of 98.07 N with 10 s dwell time. Cylindrical samples of 6 mm diameter and 8 mm length prepared by EDM cutting were used for the compression test. The surface of the compression samples was subsequently modified to the desired shape and roughness using centreless grinding. The compression tests were performed using a Zwick Z 150 device with a crosshead velocity of 0.05 s^{-1} (0.4 mm s^{-1}). Three compressive tests were performed for each sample condition. The deformability was determined from the strain as the difference between the total strain and the yield strain. A Gleeble 3800 thermomechanical tester was used for high-temperature compression tests. Cylindrical samples of 8 mm diameter and 12 mm length prepared by EDM cutting and centreless grinding were used for testing at temperatures 850, 900, 950, and 1000 °C, respectively, with an initial strain rate of 0.0001 s^{-1} (0.0012 mm s^{-1}) until a true strain of 50% was achieved. A vacuum pressure of 7 Pa was applied during the high-temperature compression tests and the heating was carried out using direct resistance heating at a rate of 6.7 °C s^{-1}. After reaching the desired temperature, the sample was held at the temperature for 120 s before the compressive test. The temperature was controlled with a thermocouple spot-welded to the specimen's surface.

3. Results

The resulting powder mixture (shown in Fig. 5) was subjected to particle size distribution (PSD) analysis by using a MasterSizer 3000 particle size analyser (see Fig. 5(c)). The designation of samples used in the present study after LPBF, HIP treatment, and HT is given in Table 2.

3.1. Chemical composition and microstructure analysis of the LPBF samples

Table 3 shows the nominal composition and the measured average chemical composition of the samples after the LPBF process (average of three 1 × 1 mm^2 area analysis from 3 different samples, 9 areas in total for each series). The results show that the chemical composition of the LPBF samples corresponds to the nominal composition, suggesting no loss of elements during the LPBF process by evaporation. Table 4 summarizes the concentration of the detected interstitial elements in the LPBF samples. The oxygen content was found to be <0.2 wt%, the nitrogen content <0.02 wt%, and the hydrogen content below the detectable limits.

The microstructure of the LPBF Ti–Al-based samples shows the presence of porosity and cracks (Fig. 6). The cracks were observed along the x direction in transversal sections and along the z direction in longitudinal sections, especially in Ti- and V-depleted areas. Pores with diameters of up to 200 μm were observed. The samples printed with a lower power of 80 W show a high volume of porosity (4.3 ± 1.5 vol%), which is in accordance with the published reports.[42–44] With increasing laser power, the concentration of porosity decreases; however, the difference is not significant. The BSE images reveal that the LPBF samples do not show complete melting of Ti-based powders, as bright circular areas rich in Ti with a size similar to that of the input Ti-based powder particles are observed (Fig. 6e, f and Table 5). It can also be observed that with an increase in the laser power from 80 W to 100 W, the volume of bright Ti-rich areas decreases. In addition, along with bright areas (marked as 1 and 2 in the BSE images), dark and grey regions are also observed, suggesting a non-homogeneous distribution of microstructure. Since the laser scan speed was 1400 mm s^{-1}, sufficient time was not offered for the homogenization of the melt (due to extreme cooling and solidification conditions).

3.2. Microstructure after HIP

Fig. 7 shows the microstructures of the HIP samples (HIP_1 (1200 °C/2h/150 MPa) and HIP_2 (1240 °C/2 h/150 MPa)), where a significant crack and porosity closure can be observed.

© 2025 The Author(s). Published by the Royal Society of Chemistry

Open Access Article. Published on 28 October 2025. Downloaded on 6/20/2026 5:31:48 PM.
This article is licensed under a Creative Commons Attribution 3.0 Unported Licence.

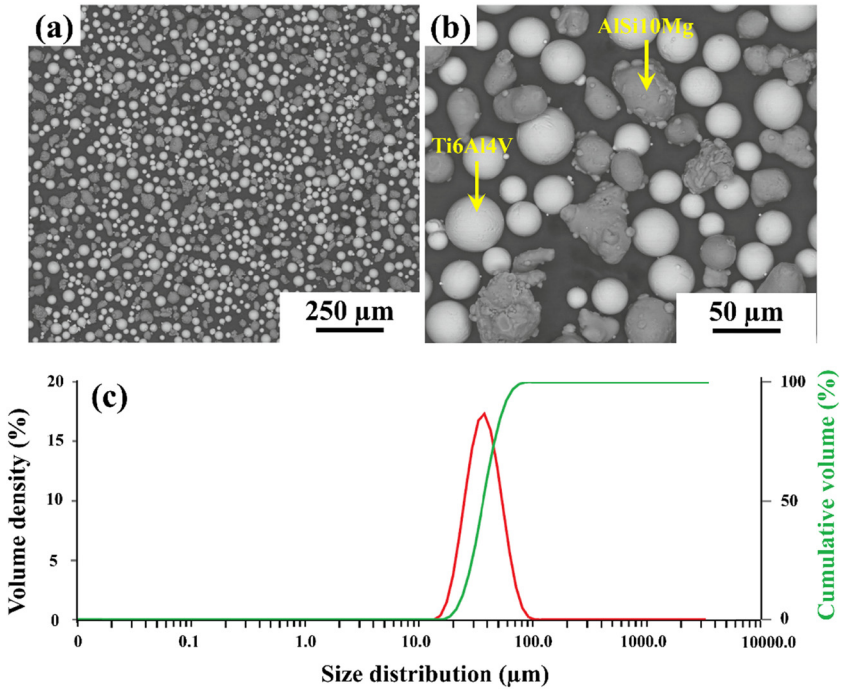

Fig. 5 (a) and (b) Backscattered scanning microscopy images of the Ti6Al4V and AlSi10Mg powder mixtures and (c) their particle size distribution (D_{50} = 37 µm).

Table 2 The nomenclature of the samples used in the present study after the LPBF process, HIP treatment, and heat treatment

Sample designation	As-printed state	After HIP	After HIP and HT
80 W – chessboard	80 W_CH	80 W_CH_HIP_1	80 W_CH_HIP_1 + HT
100 W – chessboard	100 W_CH	100 W_CH_HIP_1	100 W_CH_HIP_1 + HT
		100 W_CH_HIP_2	100 W_CH_HIP_2 + HT
100 W – meander	100 W_CH	100 W_CH_HIP_2	100 W_CH_HIP_2 + HT

Table 3 The chemical composition (both nominal and measured chemical composition) of the initial Ti–Al-based powder mixture and LPBF samples (as a function of different laser power) and detected porosity levels in LPBF samples

	Composition (at%)					
Sample designation	Ti	Al	V	Mg	Si	Porosity (%)
Nominal composition	49.8 ± 0.7	43.8 ± 0.6	1.7 ± 0.4	0.2 ± 0.1	4.5 ± 0.5	—
80 W_CH	49.8 ± 1.2	43.9 ± 1.2	1.6 ± 0.2	0.1 ± 0.1	4.6 ± 0.5	4.3 ± 1.5
100 W_CH	49.7 ± 1.1	44.2 ± 1.3	1.5 ± 0.2	0.1 ± 0.1	4.5 ± 0.6	4.1 ± 1.6
100 W_M	50.0 ± 1.0	43.8 ± 1.2	1.6 ± 0.2	0.1 ± 0.1	4.5 ± 0.7	3.8 ± 0.9

Although some pores (40 µm in size) and cracks are still observed (Fig. 7a and b), most of the cracks and pores were eliminated during the HIP treatment due to the combined application of high pressure and temperature. The volume of pores observed after HIP was found to be 0.23 ± 0.05 and 0.34 ± 0.06 vol% for the samples 80 W_CH_HIP_1 and 100 W_CH_HIP_1, respectively. A porosity of 0.20 ± 0.06 and 0.31 ± 0.04 vol% was observed for the samples 100 W_M_HIP_2 and 100 W_CH_HIP_2, respectively. The results suggest that more than 90% of pores were eliminated after the HIP process. In addition to pore elimination, the HIP process also influences the microstructure significantly. Bright spherical areas (Fig. 6e and f) corroborating the unmelted Ti-particles are no longer observed. This suggests that the simultaneous application of temperature and pressure during the HIP process activates the diffusion, allowing Ti to diffuse into its surroundings. However, still, complete homogenization of the microstructure is not observed, where two different contrasts are observed (both bright and dark contrast under BSE mode in Fig. 7). The X-ray diffraction (XRD) pattern (Fig. 8) shows the presence of γ-TiAl, α_2-Ti_3Al, and Ti_5Si_3 phases after HIP. The HIP process takes place at 1200 °C and 1240 °C, respectively, which lies in

Open Access Article. Published on 28 October 2025. Downloaded on 6/20/2026 5:31:48 PM. This article is licensed under a Creative Commons Attribution 3.0 Unported Licence.

Table 4 The average chemical concentration of the interstitial elements in the as-printed LPBF Ti–Al-based samples measured by the combustion method

Chemical composition (wt%)		
O	N	H
0.167 ± 0.033	0.013 ± 0.003	<0.005

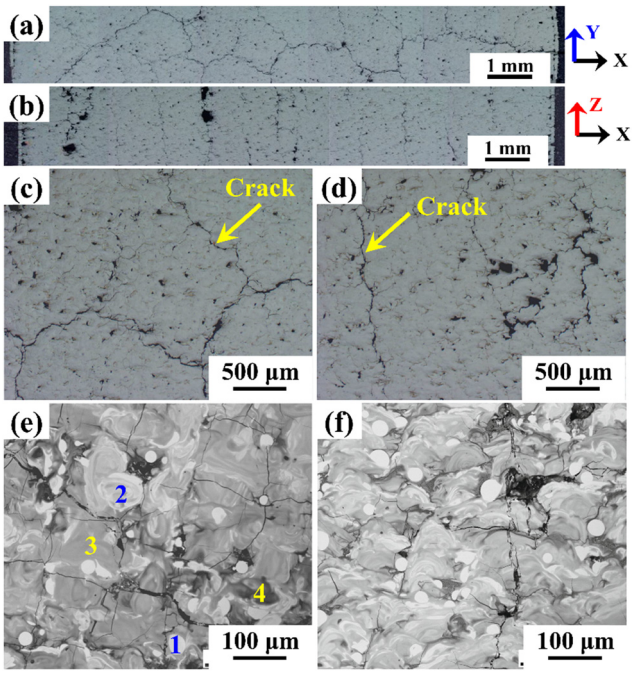

Fig. 6 The microstructure of the LPBF Ti–Al-based samples as a function of laser power and hatch style: (a) optical microscopy (OM) image of the 100 W_CH sample along the transverse direction, (b) OM image of the 100 W_CH sample along the longitudinal direction, (c) OM image of the 80 W_CH sample along the transverse direction, (d) OM image of the 100 W_M sample along the longitudinal direction, (e) backscattered scanning electron microscopy (SEM/BSE) image of the 100 W_CH sample along the transverse cut direction, and (f) SEM/BSE image of the 80W_CH sample along the longitudinal direction.

the characteristic two-phase region (α + γ) of the Ti–Al binary diagram at ∼45 at% Al. The chemical composition of the phases taken from Fig. 7f and g is shown in Table 6. The EDS results show that the bright areas correspond to the Ti-enriched α phase and the dark areas correspond to the γ phase. The pores are generally associated with the dark γ regions. The disordered α phase subsequently transforms into the ordered α_2 + γ phase during cooling as in the case of cast TiAl-based alloys.[7,45] Fine precipitates of <1 μm can be observed at higher magnifications and are identified as Ti_5Si_3 phases (based on the Ti–Al–Si ternary diagram[46]). In addition, the microstructure also shows spherical regions with a higher Al concentration than in the surrounding TiAl (Fig. 7c–f and Table 6). This may be attributed to the differences in the solubility limit of Si, where lower Si is observed in these Al-rich regions than in the surrounding γ-TiAl phase. However, the differences in the Ti, Al, and V contents compared to the TiAl matrix do not vary much and still correspond to the γ-TiAl phase. Hence, it can be assumed that the γ-TiAl phase forms during HIP by transforming the Al-rich areas after LPBF. After HIP, the samples fabricated under different processing parameters during LPBF do not show significant variations in their microstructure (Fig. 7c–f).

3.3. Microstructure after HIP and heat treatment (HT)

The samples after HIP were heat treated at temperatures corresponding to the α region of the Ti–Al binary diagram (for Al content at ∼45 at%) to homogenize and modify the microstructure to a near lamellar type. Fig. 9 shows the microstructure of samples after HIP and HT. From the XRD plot in Fig. 8, it can be observed that γ-TiAl, α_2-Ti_3Al, and Ti_5Si_3 phases coexist. The sample after HT consists of a γ-TiAl matrix with uniformly distributed Ti_5Si_3 precipitates and several lamellar grains of γ-TiAl and α_2-Ti_3Al composition with Ti_5Si_3 precipitates (Fig. 9c–f). These lamellae are formed during HT and mainly in the Ti-rich α regions. It can be observed that these lamellar grains have lower concentrations of Ti_5Si_3 precipitates than the γ-TiAl matrix. Changes in the process parameters or the HIP temperature do not significantly alter the concentration and size of these precipitates. Spherical regions with higher Al content were still observed in the microstructure indicating that the employed temperature (1370 °C) and time (20 min) during HT were insufficient to induce solid-state transformation. Comparing Fig. 7 and 9, it can be observed that the HT process coarsens the precipitates, where their size increases from 0.70 ± 0.27 μm after HIP to 2.0 ± 0.78 μm after HIP and HT, respectively. Hence, the resulting microstructure can be described as a multiphase microstructure with a high portion of the γ phase and Ti_5Si_3 precipitates along with traces of the α_2 phase. The low concentration of the α_2 phase may be attributed to the precipitation of Ti_5Si_3. The formation of a relatively high content of Ti_5Si_3 precipitates (18.0 ± 0.4 vol%) consumes a high proportion of Ti and depletes the surrounding matrix. This then leads to a shift in the chemical composition

Table 5 The average chemical composition observed in different marked areas from Fig. 6e

	Chemical composition (at%)				
Measured area	Al	Mg	Si	Ti	V
1 – unmelted Ti6Al4V particles	17.2 ± 3.2	0.1 ± 0.1	1.0 ± 0.9	79.9 ± 3.4	1.8 ± 1.1
2 – partially melted Ti6Al4V particles	36.6 ± 6.3	0.2 ± 0.2	3.3 ± 1.4	58.3 ± 5.5	1.6 ± 1.0
3 – grey area	54.1 ± 4.3	0.4 ± 0.3	5.6 ± 2.2	38.8 ± 4.1	1.1 ± 0.8
4 – dark area	75.2 ± 2.9	0.6 ± 0.3	7.5 ± 1.6	16.2 ± 2.8	0.5 ± 0.4

© 2025 The Author(s). Published by the Royal Society of Chemistry

Open Access Article. Published on 28 October 2025. Downloaded on 6/20/2026 5:31:48 PM.
This article is licensed under a Creative Commons Attribution 3.0 Unported Licence.

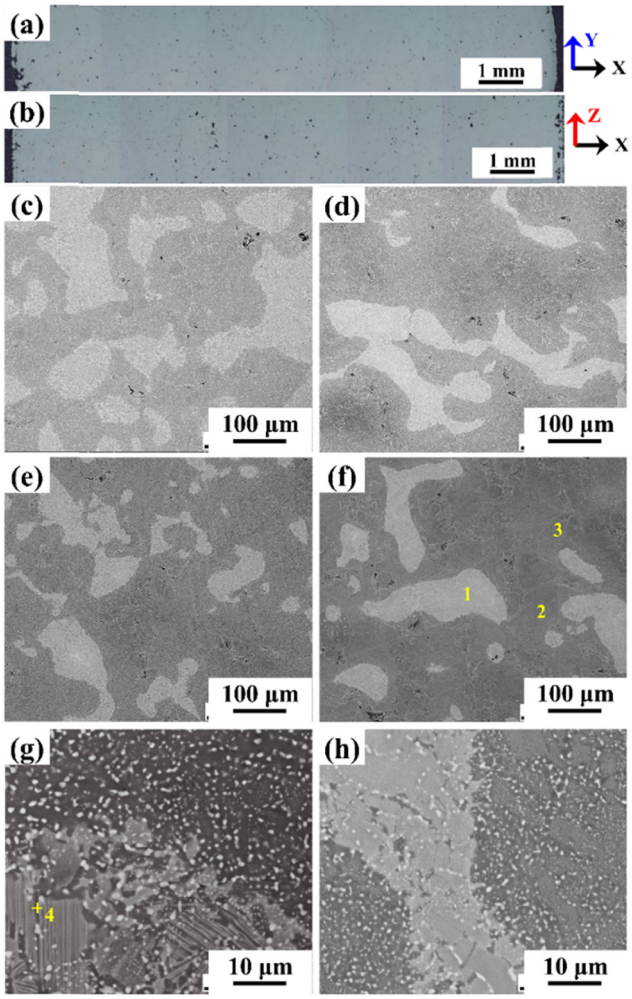

Fig. 7 Microstructure of samples after HIP treatment: optical microscopy images of the (a) 100 W_M_HIP_2 sample along the transverse direction, (b) 100 W_M_HIP_2 sample along the longitudinal direction, and (c) 100 W_CH_HIP_2 sample along the transverse direction. Backscattered electron microscopy images of the samples along the transverse direction: (d) 100 W_M_HIP_2, (e) 80 W_CH_HIP_1, (f) 100 W_CH_HIP_1, (g) 100 W_M_HIP_2, and (h) 100 W_CH_HIP_1.

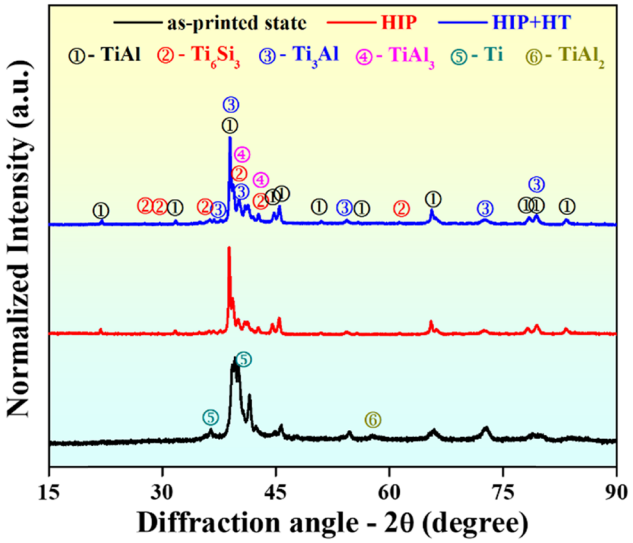

Fig. 8 The X-ray diffraction patterns of the LPBF TiAl sample in the as-printed state (black), after the HIP process (red), and after HIP + HT (blue).

of the matrix to lower Ti and higher Al contents, leading to the presence of a higher volume of the γ-TiAl phase (Table 7).

3.4. Mechanical properties at room temperature (RT)

The samples were subjected to hardness and compressive tests to assess the RT mechanical properties and anisotropy, which is typical for materials fabricated by LPBF.[47,48] The hardness tests were performed in both transverse (marked as perpendicular) and longitudinal (marked as parallel) directions. Compression tests were carried out in both parallel and perpendicular directions to the LPBF-built direction. The hardness values range between 240 HV and 260 HV (Table 8) for the studied samples under different processing conditions.

It can be observed that the samples along the perpendicular direction show higher hardness than the samples measured in the parallel direction, showing local anisotropy in the LPBF samples.[47] A higher temperature during HIP (HIP_2 process) slightly reduces the anisotropy. The use of a meander hatch offers relatively high hardness compared to the chessboard hatch style, corroborating the published results.[49]

Fig. 10 shows the representative engineering strain–stress compressive curves for the samples prepared under different conditions and after HT and their data are summarized in Table 9. The compressive curve can be divided into three different stages: initial straight-line elastic stage, non-linear plastic stage, and final failure stage. Relatively high yield strength (~550–600 MPa) was observed and the changes in the LPBF parameters or HIP temperature did not affect the properties significantly. However, significant changes in the compressive strength and deformability values may be observed. The highest compressive strength was observed for the 100 W_M_HIP_2 + HT sample with good deformability. The difference in deformability and strength values may be attributed to the presence of pores in these samples. Anisotropic behaviour was observed in all the samples, as the mechanical properties in the perpendicular direction is higher than in the parallel direction despite applying HIP and HT.

3.5. High temperature compression tests

Since TiAl-based alloys are designed for high-temperature applications (>700 °C), high-temperature compression tests were performed on selected prepared samples (80 W_CH_HIP_1 + HT). Fig. 11 shows the compressive behaviour of the 80 W_CH_HIP_1 + HT sample as a function of testing temperature. As expected, the flow stress is very sensitive to deformation temperature and decreases significantly with increasing temperature. The deformation takes place under two stages, *i.e.*, work hardening and dynamic softening, which are divided by the point characterizing the maximum compressive strength at the given temperature. The compressive strength of the tested samples was observed to be 490 MPa, 350 MPa, 250 MPa, and 160 MPa for the samples tested at 850 °C, 900 °C, 950 °C, and 1000 °C, respectively.

Open Access Article. Published on 28 October 2025. Downloaded on 6/20/2026 5:31:48 PM. This article is licensed under a Creative Commons Attribution 3.0 Unported Licence.

Table 6 The average chemical composition of the different areas measured in the sample after the HIP process from Fig. 7f and g

	Chemical composition (at%)				
Measured area	Al	Mg	Si	Ti	V
1 – bright area	40.6 ± 1.1	0.2 ± 0.2	2.8 ± 0.7	54.2 ± 1.2	2.2 ± 0.6
2 – grey area	46.7 ± 1.3	0.3 ± 0.2	4.7 ± 0.9	46.9 ± 1.2	1.4 ± 0.4
3 – spherical grey area	51.0 ± 1.1	0.3 ± 0.2	2.5 ± 0.7	45.1 ± 1.0	1.1 ± 0.4
4 – bright precipitates	12.9 ± 3.9	0.6 ± 0.5	25.1 ± 4.2	59.6 ± 4.3	1.8 ± 0.5

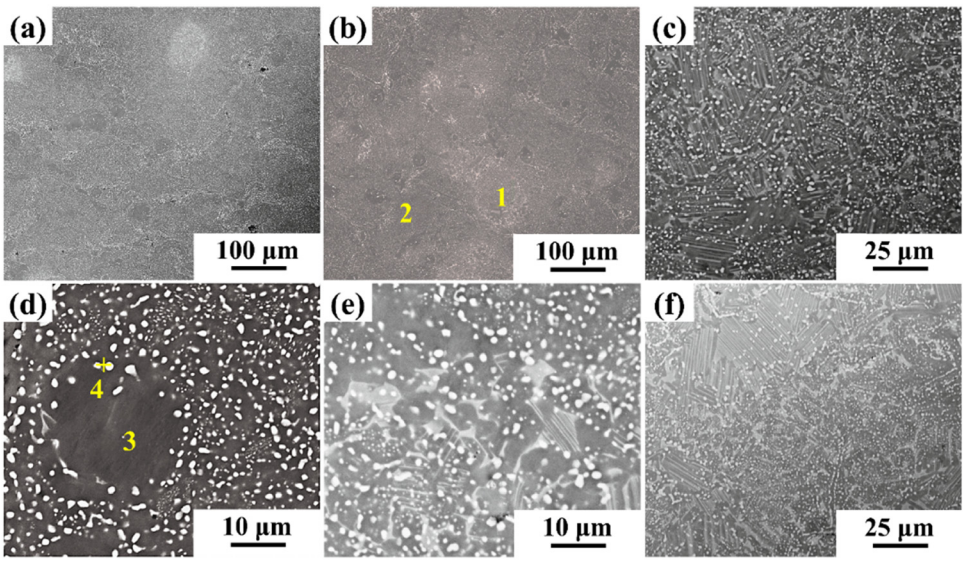

Fig. 9 Backscattered scanning electron microscopy of microstructures of samples after HIP and HT: (a) 80 W_CH_HIP_1 sample along the longitudinal direction, (b) 100 W_CH_HIP_1 sample along the longitudinal direction, (c) 100 W_CH_HIP_2 sample along the transverse direction, (d) 100 W_M_HIP_2 sample along the longitudinal direction, (e) 100 W_M_HIP_2 sample along the transverse direction, and (f) 100 W_CH_ HIP_1 sample along the transverse direction.

Table 7 The chemical composition of individual microstructural features shown in Fig. 9b and d

	Chemical composition (at%)				
Measured area	Al	Mg	Si	Ti	V
1 – bright area	43.2 ± 2.7	0.2 ± 0.1	3.0 ± 0.9	51.9 ± 2.6	1.7 ± 0.3
2 – grey area	43.8 ± 2.5	0.2 ± 0.1	5.0 ± 1.0	49.2 ± 2.5	1.8 ± 0.4
3 – spherical grey area	46.7 ± 1.9	0.2 ± 0.1	1.3 ± 0.6	50.8 ± 2.1	1.0 ± 0.2
4 – bright precipitates	10.9 ± 2.4	0.2 ± 0.1	30.8 ± 3.8	56.7 ± 3.0	1.4 ± 0.5

Table 8 The Vickers hardness (HV10) values observed for the TiAl-based samples after HIP and HT

Sample direction	80 W_CH_HIP_1 + HT	100 W_CH_HIP_1 + HT	100 W_CH_HIP_2 + HT	100 W_M_HIP_2 + HT
Perpendicular	242 ± 5	260 ± 22	238 ± 21	261 ± 21
Parallel	210 ± 17	242 ± 8	238 ± 28	249 ± 19

4. Discussion

4.1. Laser beam powder bed fusion of the mixture

Research studies have been devoted to *in situ* alloy formation from elemental powder blends using LPBF, *e.g.*, Ti_2AlNb intermetallic alloy,[35] TiNbMoTaW refractory bio-high entropy alloy,[37] Ti–26Nb,[51] Ti_3Al-based intermetallics,[52] NiTi,[53] *etc.* Most of these studies show that elemental powders can be used for the fabrication of structural alloys. However, even with the use of atomized pre-alloyed powders, external defects like porosity strongly depend on the volumetric energy density. The volumetric energy density '*E*' can be expressed as

$$E = \frac{P}{v \cdot h \cdot t}\left[\mathrm{J\ mm^{-3}}\right] \quad (1)$$

© 2025 The Author(s). Published by the Royal Society of Chemistry

Open Access Article. Published on 28 October 2025. Downloaded on 6/20/2026 5:31:48 PM.
This article is licensed under a Creative Commons Attribution 3.0 Unported Licence.

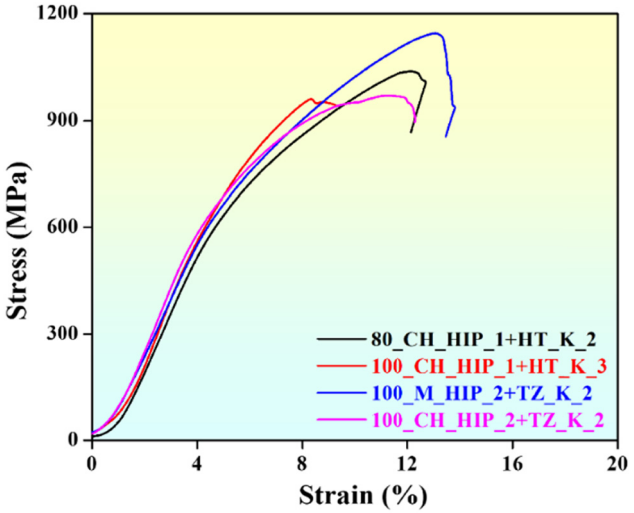

Fig. 10 Plot showing the room temperature compressive engineering stress–strain curves of LPBF Ti–Al-based samples after HIP and HT (tested along the perpendicular direction to the built direction).

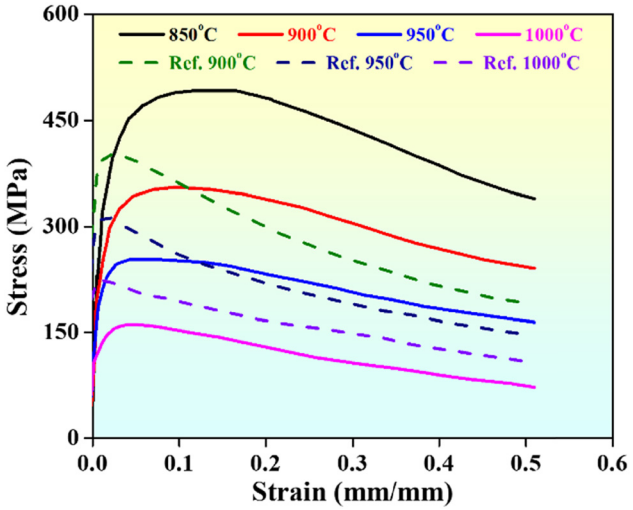

Fig. 11 Compressive true stress–true strain curves tested for the 80 W_CH_HIP_1 + HT sample as a function of different testing temperatures and in comparison with Ti–43Al–8Nb–3.6C–0.7Mo tested under similar conditions.[50]

where 'P' is the laser power, 'v' is the laser scanning speed, 'h' is the hatch distance, and 't' corresponds to the layer thickness.[42] Lower energy densities may lead to significant porosity, and higher energy densities may lead to crippling of the surface due to irregular layers.[51] However, in the present case (Ti-based and Al-based powder mixture), the exothermic reaction also influences the LPBF process. Ti has a higher melting point than Al, allowing the Al-based powder to melt first. The Al-melt then reacts with the Ti powder with a significant release of heat. Bizot *et al.*[54] reported in detail the reaction between Ti and Al, suggesting a self-sustaining melting behaviour until the reaction is complete. The dissolution step is limited by the low solubility of Ti in Al and the formation of the intermetallic compound ($TiAl_3$).[54] In the present study, very low energy densities of 23.8 (80 W) and 29.8 J mm^{-3} (100 W) were employed due to high scanning speed and low laser power. Buhairi *et al.*[55] determined the energy density for ideal melting of unit volume Ti6Al4V as 55–65 J mm^{-3}, which is higher than the energy density employed in the present study. However, the amount of unmelted Ti6Al4V powder in the microstructure ranges from 8 to 11%, indicating a non-negligible influence of the exothermic reaction. Assuming that Al melts rapidly first, followed by an exothermic reaction with Ti, this should ideally result in the formation of a melt pool, which upon solidification produces the γ-TiAl and α phases. However, the unmelted Ti phase is observed in the solidified sample showing signs of inhomogeneity both in the melt pool and after solidification.

Fig. 12 shows a typical melted pool microstructure after LPBF of the powder mixture along with the EDS concentration profile indicating a compositional inhomogeneity (especially in the lower part of the melt pool, where usually remelting takes place). Inhomogeneities were observed mainly near unmelted or partially melted Ti6Al4V particles. Fig. 13a and b shows the microstructure of LPBF samples fabricated at the following process parameters: P = 125 W, v = 1400 mm s^{-1}, h = 0.12 mm and P = 100 W, v = 900 mm s^{-1}, h = 0.12 mm, respectively. It may be observed that even when higher power and lower scanning speed were employed, the microstructure was still not completely homogeneous, and unmelted Ti6Al4V particles were present. Even with lower scanning speeds (400 mm s^{-1}) and smaller hatch distances (0.09, 0.045 mm), the unmelted particles cannot be eliminated. However, the content of unmelted Ti6Al4V decreased (higher than 5%). On the other hand, the parameters used (P = 120 W, v = 900 mm s^{-1}, and h = 0.09 mm) yield a theoretical energy density of 74.1 J mm^{-3}, which should be sufficient for melting Ti. Reports suggest that the heat and mass transport observed in the LPBF melt pool was driven by Marangoni convection,

Table 9 Compressive properties of LPBF Ti–Al-based samples at room temperature after HIP and HT (PER: perpendicular direction, PAR: parallel direction)

	Yield strength (MPa)		Compressive strength (MPa)		Deformability (%)	
Sample designation	PER	PAR	PER	PAR	PER	PAR
80 W_CH_HIP_1 + HT	604 ± 16	576 ± 26	1034 ± 82	922 ± 42	7.91 ± 1.42	6.30 ± 1.85
100 W_CH_HIP_1 + HT	589 ± 18	549 ± 13	991 ± 32	947 ± 27	4.55 ± 0.45	4.53 ± 1.38
100 W_CH_HIP_2 + HT	574 ± 24	566 ± 42	924 ± 43	860 ± 42	4.32 ± 0.71	3.23 ± 1.02
100 W_M_HIP_2 + HT	602 ± 32	590 ± 33	1054 ± 81	1010 ± 99	7.95 ± 0.97	7.69 ± 1.35

Open Access Article. Published on 28 October 2025. Downloaded on 6/20/2026 5:31:48 PM.
This article is licensed under a Creative Commons Attribution 3.0 Unported Licence.

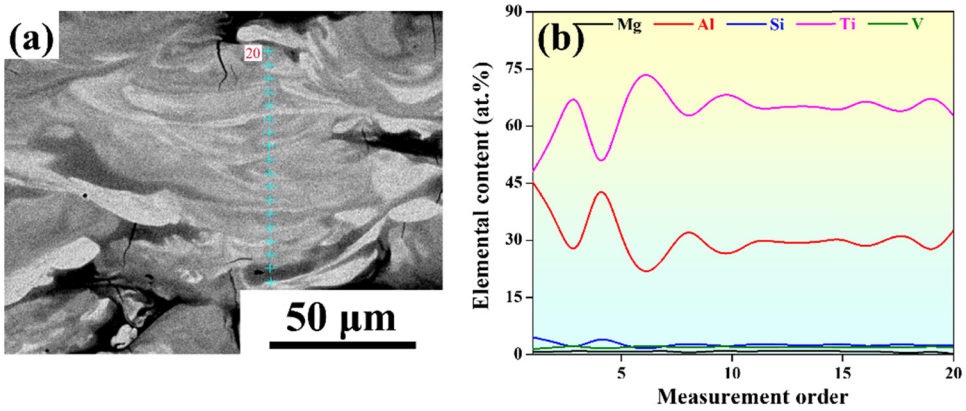

Fig. 12 (a) Micrograph showing the melt pool features observed in the LPBF 100 W_CH sample along the longitudinal direction and (b) energy dispersive spectroscopy concentration profile showing the elemental distribution.

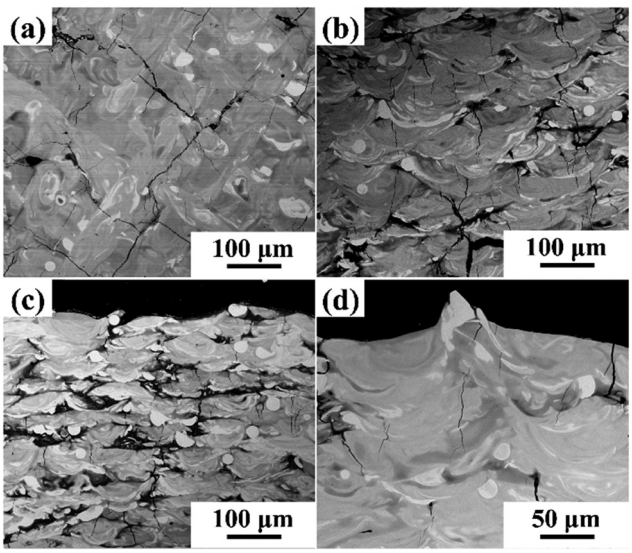

Fig. 13 Backscattered scanning electron microscopy images of the LPBF samples as a function of process parameters: (a) P = 125 W, S = 1400 mm s^{-1}, h = 0.12 mm, transverse direction, (b) P = 100 W, S = 900 mm s^{-1}, h = 0.12 mm, longitudinal direction, (c) P = 100 W, S = 900 mm s^{-1}, h = 0.12 mm, longitudinal direction, and (d) P = 120 W, S = 450 mm s^{-1}, h = 0.12 mm, longitudinal direction, showing the presence of unmelted Ti particles along their surface.

evaporation, and resulting recoiling pressure on the surface of the melt pool.[56,57] Moreover, it has been observed that the gas flow affects the height of the melt track, and the extent of denudation significantly influences the quality of LPBF parts. The gas stream drags particles into the process zone and moves the particles towards the edges of the melt pool. The particles are either incorporated into the melt pool or present on the surface. Fig. 13c and d shows the adhered Ti6Al4V particles on the surface of the LPBF parts corroborating the influence of denudation during the LPBF. In addition, the particles dragged toward the melt pool surface remain in the melt pool unmelted.[56,57] Hence, employing higher energy densities increases the possibility of melting the Ti6Al4V powder, but also causes higher denudation. The denudation results in the formation of porosity, which is usually in the vicinity of unmelted Ti powder particles present between the scan traces (Fig. 6e). Local melt turbulences may lead to uneven layer width (Fig. 6f), leading to porosity formation.

Another problem associated with LPBF processing of the Ti- and Al-based powder mixture is cracking. Lee *et al.*[58] observed that during the fabrication of LPBF Ti48Al–2Cr–2Nb, solidification and thermal cracks are observed in all keyhole, transition, and conduction modes. Thermal cracks are caused by large thermal stresses at temperatures below the ductile-to-brittle transition. In addition, it was observed that the energy density influences the crack spacing during transition and conduction modes.[58] The crack spacing increases with increasing energy density, a phenomenon also observed in the present study (Fig. 14(a)). The microstructure shown in Fig. 14(a) reveals large horizontal cracks, approximately 3 mm in length, connecting adjacent pores. These extended horizontal cracks at higher energy densities lead to warping and distortion of the fabricated parts. As depicted in Fig. 14(b), warping is predominantly observed in samples produced at higher energy densities. In fact, at these elevated energy densities, the fabrication process had to be halted due to severe warping. Only the lower energy densities listed in Table 1 allowed for the successful preparation of samples with the specified dimensions; however, even at these lower densities, smaller cracks and pores were still present. Given the presence of cracks and other internal defects in the fabricated samples, the application of hot isostatic pressing (HIP) becomes essential to enhance their structural integrity. The information provided, in line with other publications,[35–37] suggests that to achieve an appropriate microstructure, homogeneity and elimination of defects during *in situ* alloying of LPBF, a comprehensive approach is needed, including precise control of printing parameters and scanning strategies. However, it is necessary to approach individually for the chemical compositions used and assume different behaviour of powders with individual chemical elements in terms of phase transformation temperatures, reactivity and density. While the present study utilized a relatively low energy input in the LPBF process followed by HIP to achieve full densification and a tailored microstructure, it is worth noting that

© 2025 The Author(s). Published by the Royal Society of Chemistry

Open Access Article. Published on 28 October 2025. Downloaded on 6/20/2026 5:31:48 PM. This article is licensed under a Creative Commons Attribution 3.0 Unported Licence.

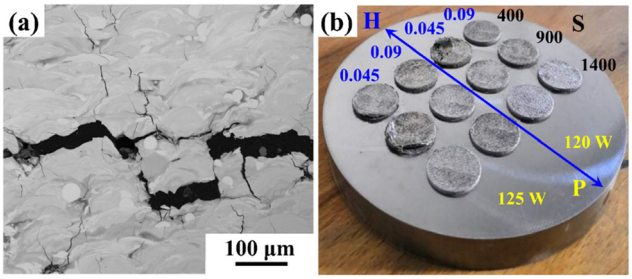

Fig. 14 (a) Example of horizontal cracking in the sample after LPBF (P = 120 W, S = 900 mm s^{-1}, h = 0.12 mm, longitudinal cut (SEM/BSE). (b) Example of warping when inappropriate parameters are used during LPBF (h – hatch spacing (mm), v – scan speed (mm s^{-1}), P – laser power).

alternative approaches based on process optimization at higher energy inputs can also lead to high-density TiAl parts without post-processing. For instance, Park *et al.*[59] demonstrated that by optimizing hatch spacing in a β-solidifying γ-TiAl alloy, relative densities above 99% could be achieved directly during LPBF, while simultaneously refining columnar β grain structures and minimizing cracking. Similarly, Löber *et al.*[60] showed that careful control of scanning parameters and energy density can result in crack-free, dense TiAl builds even in the absence of HIP.

However, these studies relied on pre-alloyed powders, which typically exhibit more predictable melting and solidification behaviour than mixed or elemental powders used for *in situ* alloying. In our case, the powder mixture of Ti6Al4V and AlSi10Mg introduces additional complexity in terms of compositional homogenization and phase formation, which cannot be adequately addressed by process parameter optimization alone. As such, HIP post-processing was essential to eliminate residual porosity, relieve internal stresses, and promote microstructural uniformity and desirable phase distributions. Therefore, the choice of a low-energy LPBF strategy followed by HIP represents a suitable compromise in the context of *in situ* alloying, where the benefits of enhanced flexibility and cost-effective feedstock are balanced against the need for controlled post-processing to achieve structural and functional integrity.

4.2. Effect of hot isostatic pressing on homogeneity, and crack and porosity elimination

HIP helps remove solidification porosity of cast materials.[61] During HIP, the parts are heated in an inert atmosphere with isostatic pressure making the material plastic allowing void closure under pressure. In addition, the microstructure homogenizes with the application of pressure and temperature. However, high temperature and long dwell during HIP also decrease the mechanical properties due to grain coarsening.[62] The effect of HIP on the homogeneity of the 80 W_CH sample can be observed in Fig. 15, where the EDS line scan results confirm the same. The EDS line scan profile of the LPBF samples shows significant variation in the composition (both Ti and Al) due to the presence of unmelted Ti-particles and the presence of $TiAl_2$ and $TiAl_3$ phases. However, after HIP, these chemical deviations were significantly reduced, and the concentration of Ti and Al stabilizes between 40 and 60 at%. In addition, elimination of pores and cracks can be observed after HIP. The density of the LPBF sample was found to be $\sim 3.83 \pm 0.04$ g cm^{-3} and the density increases by 2.5% ($\sim 3.93 \pm 0.01$ g cm^{-3}) after HIP. However, after HIP, complete elimination of pores was not observed.

Fig. 7, 9, and 15 show the presence of residual porosity in the γ-TiAl phase where the highest amount of Ti_5Si_3 precipitates was observed. The Ti_5Si_3 precipitates were characterized by high hardness[39] and high temperature stability.[63] Hence, the

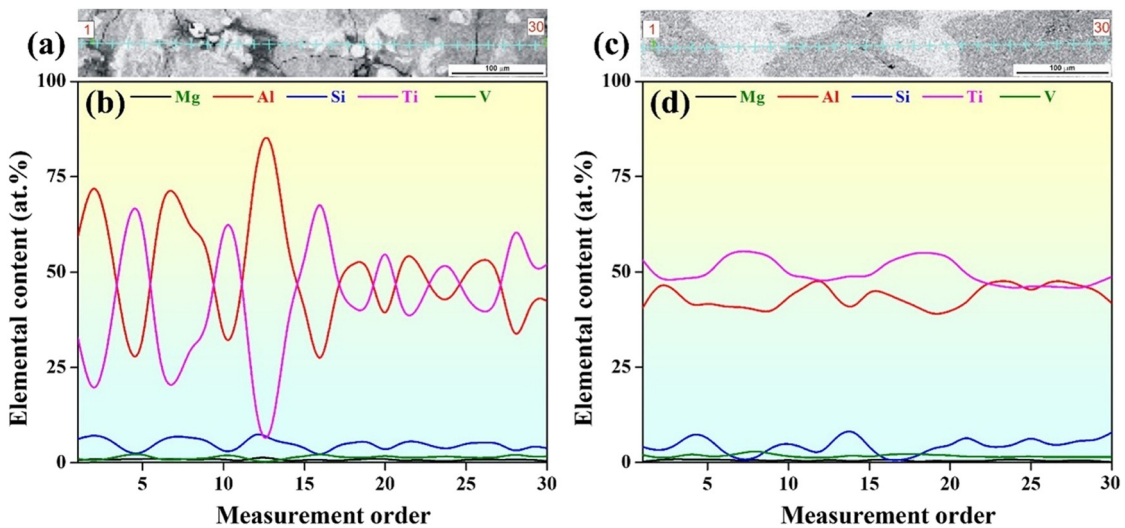

Fig. 15 Energy dispersive concentration profiles of the alloying elements: (a) position of measurement points during the line analysis at a transversal section of the 80W_CH sample under the as-printed condition, (b) concentration profile of elements in the 80W_CH sample under the as-printed condition, (c) position of measurement points during the line analysis at a transversal section of the 80 W_CH sample after HIP and (d) concentration profile of elements in the 80 W_CH sample after HIP.

Open Access Article. Published on 28 October 2025. Downloaded on 6/20/2026 5:31:48 PM.
This article is licensed under a Creative Commons Attribution 3.0 Unported Licence.

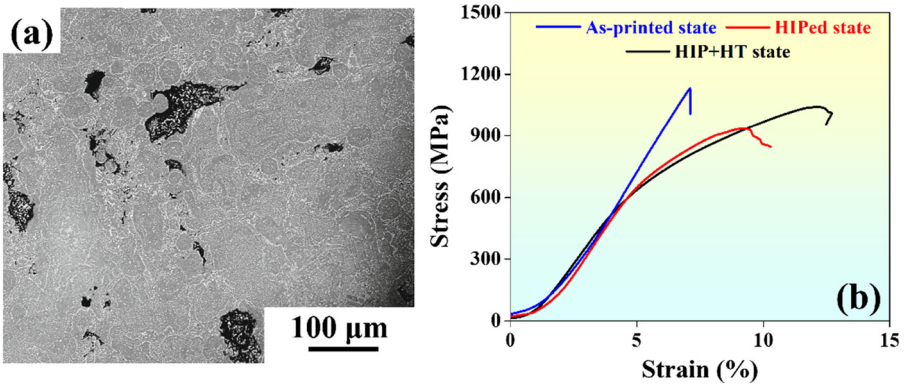

Fig. 16 (a) Backscattered scanning electron microscopy image of the 80 W_CH sample along the transverse direction after application of HT and the subsequent HIP_1 process. (b) Room temperature compressive stress–strain plot of the 80 W_CH sample tested under different conditions.

incomplete elimination of pores during HIP may be attributed to the presence of hard Ti_5Si_3 precipitates. To address this issue, one 80 W_CH sample was subjected to heat treatment (HT) alone, followed by hot isostatic pressing (HIP) under the HIP_1 condition. The resulting microstructure is shown in Fig. 16(a). As observed, the HIP process had minimal effect on porosity reduction, with the pore content remaining around 3 vol%, a value comparable to that observed after laser powder bed fusion (LPBF). Ti_5Si_3 precipitates were found within most of the larger pores, hindering pore elimination due to their low plasticity. This observation was further corroborated by density measurements using a gas pycnometer, which showed a slight increase in density from 3.83 ± 0.04 to only 3.87 ± 0.02 after HIP following HT.

The varying frequency of Ti_5Si_3 precipitates across different microstructural regions after the HIP process can be attributed to the differing solubility of Si in the phases present. At 1200 °C (the temperature used during HIP), Si exhibits the highest solubility in the Ti_3Al phase and the α phase (approximately 1.5 at%), a lower solubility in the γ-TiAl phase (around 0.5 at%), and the lowest solubility in the $TiAl_2$ phase (around 0.25 at%).[64]

4.3. Effect of HIP and HT on mechanical properties

Reports show that the hardness of the as-cast or powder metallurgy-fabricated Ti–Al-based alloys after HIP and heat treatment generally ranges between 300 HV and 400 HV.[4,65–67] However, the alloys in the reports were alloyed with refractory metals (Nb, Mo, Cr) and generally show a fully lamellar or nearly lamellar microstructure (higher content of the harder α_2 phase compared to the softer γ phase).[66–68] Hence, solid solution hardening by refractory metals and higher contents of the hard α_2 phase increases the hardness of these alloys. For instance, Perdrix *et al.*[69] reported a hardness of ∼280 HV for a binary Ti–48Al (at%) alloy prepared by levitation melting, and Youn *et al.*[70] observed a hardness of ∼250 HV for a Ti–48Al–2Cr–2Nb alloy fabricated by the EPBF process. Both alloys showed near gamma or duplex microstructures. Hence, the hardness values of the present material match the hardness values of the other TiAl-based alloys with a duplex or nearly gamma microstructure. Thus, the fine Ti_5Si_3 precipitates do not significantly increase the hardness, unlike Ti_5Si_3 silicides in as-cast TiAl alloys with higher Si contents.[39]

The yield strength of the samples in this study was 560–600 MPa. In comparison, the Ti4822 alloy (Ti–48Al–2Cr–2Nb) prepared from atomized powders using EPBF showed a yield strength of ∼480 MPa at RT,[70,71] which is ∼20% lower than that of the present study. Similar yield strength values are also reported by Boehlert *et al.* (475–550 MPa) for the Ti–45Al–2Nb–2Mn–0.8TiB2 alloy with a duplex microstructure prepared from atomized powders using HIP.[72] The deformability values of the present alloy are lower than the values of most cast and forged TiAl-based alloys. However, they are comparable with the values published by Wei Li *et al.*[73,74] for LPBF Ti–43.5Al–6.5Nb–2Cr–0.5B and LPBF Ti–46.5Al–2.5Cr–2Nb–0.5Y alloys, Löber *et al.*[60] for the LPBF TNM-B alloy, and Huang *et al.*[28] for LPBF Ti–44Al–4Nb–1Mo–1Cr. Löber *et al.*[60] reported a relative density of 98.89–99.46% with pore size ranging between 20 and 50 µm for the LPBF TNM-B alloy. Hence, it may be assumed in this study that the deformability is affected by residual porosity (0.2–0.3 vol%) and it cannot be eliminated during HIP treatment.

The results of compression tests showed that the prepared material has relatively high strength values at high temperatures. Fig. 11 also shows the compressive behaviour of the Ti–43Al–8Nb–3.6C–0.7Mo alloy reinforced with Ti_2AlC carbide particles with a near gamma microstructure prepared by centrifugal casting[50] and tested with the same deformation rate and temperature (except 850 °C). It may be observed that the strength of the carbide-reinforced composite is higher than that of the present material at all tested temperatures. However, it should be noted that the Ti–43Al–8Nb–3.6C–0.7Mo alloy is alloyed with refractory metals (Nb, Mo), which increases the high-temperature resistance. In addition, the addition of carbon and carbide reinforcement also increases their strength. The high-temperature resistance of the present material is comparable to that of low-alloyed TiAl alloys with a duplex or near gamma microstructure and to that of the LPBF Ti–48Al–2Cr–2Nb.[70–72,75]

The engineering strain–stress curves for the 80 W_CH sample in the LPBF state, after HIP, and after HIP and HT

© 2025 The Author(s). Published by the Royal Society of Chemistry

Open Access Article. Published on 28 October 2025. Downloaded on 6/20/2026 5:31:48 PM. This article is licensed under a Creative Commons Attribution 3.0 Unported Licence.

can be observed in Fig. 16b. In the as-printed state, a yield strength above 1100 MPa is observed. However, after reaching the peak value of elastic deformation, premature failure occurs due to the presence of a high content of cracks and pores without any plastic deformation. The high yield strength can be attributed to the fine microstructure, as in the case of other LPBF samples, and the supersaturated solid solution of Si in TiAl due to extreme solidification conditions.[76–81] HIP decreases the yield strength to 570–600 MPa, but the samples show a plastic deformation (deformability) of about 4–5% due to the partial elimination of defects (cracks and pores) and microstructure coarsening. The subsequent HT further decreases the yield strength (550–600 MPa) but improves the deformability to ~8%. The decrease in the yield strength can be explained by the decrease in the content of the α_2 phase with a higher content of γ-TiAl and an increase in the size of the Ti_5Si_3 precipitates.

To achieve improved strength and deformability, the ratio between Ti-based and Al-based powders may be modified (a higher concentration of Ti may be employed) to ensure a higher content of the α_2 phase and lamellar grains and a lower volume of Ti_5Si_3 precipitates, which prevents the complete elimination of pores during the HIP process. This study shows a novel strategy to process γ-TiAl-based alloys using LPBF from powder blends based on Ti and Al. This proposed and experimentally verified method enables a relatively easy and cost-effective fabrication of TiAl alloys considering the price of the feedstock powders. Due to the limitations associated with processing feedstock materials and modifying their composition, the present strategy can provide access to chemical compositions that are difficult to achieve by the atomization process. In addition, using HIP reduces cracks and pores in the LPBF-prepared TiAl alloys. The alloy fabrication in the present study shows a room temperature compressive yield strength of ~550 MPa, and a maximum strength of 490 MPa was achieved at 850 °C. Considering that this is the first study dealing with the use of a mixture of powders for the preparation of γ-TiAl-based intermetallics, reasonable mechanical properties in compression are observed even at high temperatures. Despite the progress achieved, further optimization is required before these materials can reach application readiness. In addition to the mentioned change in the ratio between Ti-based and Al-based powders, future research should focus on enhancing compositional homogeneity and phase stability by exploring refined scan strategies, moderate platform preheating, and digital process control techniques. Long-term goals will involve evaluating mechanical performance under service-relevant conditions and validating the process across other alloy families with similar volatility and complexity. These steps are crucial for progressing towards reliable, sustainable, and industrially scalable additive manufacturing of next-generation materials.

5. Conclusions

The present work investigates the microstructure, phase composition, hardness, RT, and high-temperature compressive test of the LPBF Ti–44Al–1.7V–0.2Mg–4.5Si samples fabricated from Ti6Al4V and AlSi10Mg powder mixtures and subjected to HIP and heat treatment. The main conclusions are summarized as follows:

(1) Fabrication of the Ti–44Al–1.7V–0.2Mg–4.5Si alloy using a mixture of commercially available Ti6Al4V and AlSi10Mg powders by the LPBF process is validated. It is necessary to use low power (80–100 W), higher scanning speed (around 1400 mm s^{-1}), and a hatch spacing of ~0.12 mm. However, the samples show the presence of a non-uniform microstructure with a high volume of cracks and pores. Hence, HIP was used as the post-processing step.

(2) The HIP process eliminated more than 90% of porosity and cracks and significantly homogenized the microstructure. However, 0.2–0.3 vol% of residual porosity still exists, which may be attributed to the presence of brittle Ti_5Si_3 precipitates, which promotes non-uniform plastic deformation.

(3) HIP and subsequent HT led to the modification of the microstructure to multiphase type with a high portion of the γ-TiAl phase and with the presence of coarse Ti_5Si_3 particles.

(4) The prepared alloy after LPBF, HIP, and HT showed a yield strength of 570–600 MPa and a compressive strength of 1050 MPa at RT and 490 MPa at 850 °C.

(5) Hardness, yield strength, compressive strength, and deformability are observed to be higher in the direction perpendicular to the printing direction as compared to the parallel direction, which indicates the presence of anisotropy despite the application of HIP and HT.

Author contributions

Tomas Cegan: conceptualization, data curation, visualisation, investigation, writing – original draft, writing – review and editing; Jan Jurica: data curation, visualisation, investigation; Katerina Skotnicova: supervision, investigation, writing – review and editing; Marek Pagac: methodology, investigation; Michaela Stamborska: methodology, investigation; Lukas Horsak: methodology, investigation; Jiri Hajnys: methodology, investigation; Jakub Mesicek: methodology, investigation; Konda Gokuldoss Prashanth: writing – review and editing, visualisation, supervision.

Conflicts of interest

The authors declare that they have no known competing financial interests or personal relationships that could have appeared to influence the work reported in this paper.

Data availability

The data supporting this article are available at Zenodo at **https://doi.org/10.5281/zenodo.14866468**.

Supplementary information (SI) is available. See DOI: **https://doi.org/10.1039/d5ma00139k**.

Open Access Article. Published on 28 October 2025. Downloaded on 6/20/2026 5:31:48 PM. This article is licensed under a Creative Commons Attribution 3.0 Unported Licence.

Acknowledgements

The authors acknowledge the financial support of the European Union under the REFRESH – Research Excellence for Region Sustainability and High-tech Industries project number CZ.10.03.01/00/22_003/0000048 *via* the Operational Programme Just Transition. This research was also funded by Slovak Research and Development Agency under the contract SK-CN-21-0018. The work was further supported by the project No. TN02000018 National Centre of Competence ENGINEERING, funded by the Technology Agency of the Czech Republic. The authors would also like to thank Ing. Juraj Lapin DrSc. for help with high temperature compression tests and for the valuable advice and comments.

References

1 X. Wu, Review of alloy and process development of TiAl alloys, *Intermetallics*, 2006, **14**(10–11), 1114–1122, DOI: **10.1016/j.intermet.2005.10.019**, ISSN 0966-9795.

2 B. Duan, Y. Yang, S. He, Q. Feng, L. Mao, X. Zhang, L. Jiao, X. Lu, G. Chen and Ch Li, History and development of γ-TiAl alloys and the effect of alloying elements on their phase transformations, *J. Alloys Compd.*, 2022, **909**, 164811, DOI: **10.1016/j.jallcom.2022.164811**, ISSN 0925-8388.

3 R. Xu, M. Li and Y. Zhao, A review of microstructure control and mechanical performance optimization of γ-TiAl alloys, *J. Alloys Compd.*, 2023, **932**, 167611, DOI: **10.1016/j.jallcom.2022.167611**, ISSN 0925-8388.

4 E. Schwaighofer, B. Rashkova, H. Clemens, A. Stark and S. Mayer, Effect of carbon addition on solidification behavior, phase evolution and creep properties of an intermetallic β-stabilized γ-TiAl based alloy, *Intermetallics*, 2014, **46**, 173–184, DOI: **10.1016/j.intermet.2013.11.011**, ISSN 0966-9795.

5 D. Li, G. Zhang, G. Lu, Y. Liu, J. Wang and Ch Liu, Precipitation of Ti_2Al phases at lamellar interfaces in a high-Nb-containing TiAl alloy during thermal exposure, *J. Mater. Sci. Technol.*, 2022, **126**, 132–140, DOI: **10.1016/j.jmst.2022.02.048**, ISSN 1005-0302.

6 J. Lapin, T. Pelachová and M. Dománková, Long-term creep behaviour of cast TiAl-Ta alloy, *Intermetallics*, 2018, **95**, 24–32, DOI: **10.1016/j.intermet.2018.01.013**, ISSN 0966-9795.

7 K. Kamyshnykova, J. Lapin, T. Pelachová, T. Cegan, J. Jurica and A. Volodarskaja, Microstructure and mechanical properties of Ti-45Al-2W-xC alloys, *Intermetallics*, 2022, **148**, 107618, DOI: **10.1016/j.intermet.2022.107618**, ISSN 0966-9795.

8 M. Cabibbo, A. Knaislová, P. Novák, F. Průša and C. Paoletti, Role of Si on lamellar formation and mechanical response of two SPS Ti–15Al–15Si and Ti–10Al–20Si intermetallic alloys, *Intermetallics*, 2021, **131**, 107099, DOI: **10.1016/j.intermet.2021.107099**, ISSN 0966-9795.

9 L. Song, X. Hu, L. Wang, A. Stark, D. Lazurenko, U. Lorenz, J. Lin, F. Pyczak and T. Zhang, Microstructure evolution and enhanced creep property of a high Nb containing TiAl alloy with carbon addition, *J. Alloys Compd.*, 2019, **807**, 151649, DOI: **10.1016/j.jallcom.2019.151649**, ISSN 0925-8388.

10 G. Chen, F. Yu, X. Hou, Y. Yang, B. Duan, Q. Feng, X. Zou, E. Wang, X. Hou, X. Lu and Ch Li, Performance of $BaZrO_3$/Y_2O_3 dual-phase refractory applied to TiAl alloy melting, *Ceram. Int.*, 2022, **48**(14), 20158–20167, DOI: **10.1016/j.ceramint.2022.03.294**, ISSN 0272-8842.

11 H. Zhang, X. Tang, Ch Zhou, H. Zhang and S. Zhang, Comparison of directional solidification of γ-TiAl alloys in conventional Al_2O_3 and novel Y_2O_3-coated Al_2O_3 crucibles, *J. Eur. Ceram. Soc.*, 2013, **33**(5), 925–934, DOI: **10.1016/j.jeurceramsoc.2012.11.006**, ISSN 0955-2219.

12 S. Yanqing, G. Jingjie, J. Jun, L. Guizhong and L. Yuan, Composition control of a TiAl melt during the induction skull melting (ISM) process, *J. Alloys Compd.*, 2002, **334**(1–2), 261–266, DOI: **10.1016/S0925-8388(01)01766-2**, ISSN 0925-8388.

13 K. Kamyshnykova and J. Lapin, Vacuum induction melting and solidification of TiAl-based alloy in graphite crucibles, *Vacuum*, 2018, **154**, 218–226, DOI: **10.1016/j.vacuum.2018.05.017**, ISSN 0042-207X.

14 X. Ding, L. Zhang, J. He, F. Zhang, X. Feng, H. Nan, J. Lin and Y.-W. Kim, As-cast microstructure characteristics dependent on solidification mode in TiAl-Nb alloys, *J. Alloys Compd.*, 2019, **809**, 151862, DOI: **10.1016/j.jallcom.2019.151862**, ISSN 0925-8388.

15 J.-K. Kim, J.-H. Kim, J.-Y. Kim, S.-H. Park, S.-W. Kim, M.-H. Oh and S.-E. Kim, Producing fine fully lamellar microstructure for cast γ-TiAl without hot working, *Intermetallics*, 2020, **120**, 106728, DOI: **10.1016/j.intermet.2020.106728**, ISSN 0966-9795.

16 M. Badami and F. Marino, Fatigue tests of un-HIP'ed γ-TiAl engine valves for motorcycles, *Int. J. Fatigue*, 2006, **28**(7), 722–732, DOI: **10.1016/j.ijfatigue.2005.09.004**, ISSN 0142-1123.

17 R. J. Simpkins, M. P. Rourke, T. R. Bieler and P. A. McQuay, The effects of HIP pore closure and age hardening on primary creep and tensile property variations in a TiAl XD™ alloy with 0.1 wt% carbon, *Mater. Sci. Eng., A*, 2007, **463**(1–2), 208–215, DOI: **10.1016/j.msea.2006.09.114**, ISSN 0921-5093.

18 C. Scheu, E. Stergar, M. Schober, L. Cha, H. Clemens, A. Bartels, F.-P. Schimansky and A. Cerezo, High carbon solubility in a γ-TiAl-based Ti–45Al–5Nb–0.5C alloy and its effect on hardening, *Acta Mater.*, 2009, **57**(5), 1504–1511, DOI: **10.1016/j.actamat.2008.11.037**, ISSN 1359-6454.

19 A. Couret, M. Allen, M. W. Rackel, B. Galy, J.-P. Monchoux, V. Güther, F. Pyczak, P. Sallot and M. Thomas, Chemical heterogeneities in tungsten containing TiAl alloys processed by powder metallurgy, *Materialia*, 2021, **18**, 101147, DOI: **10.1016/j.mtla.2021.101147**, ISSN 2589-1529.

20 M. N. Mathabathe, A. S. Bolokang, G. Govender, C. W. Siyasiya and R. J. Mostert, Cold-pressing and vacuum arc melting of γ-TiAl based alloys, *Adv. Powder Technol.*, 2019, **30**(12), 2925–2939, DOI: **10.1016/j.apt.2019.08.038**, ISSN 0921-8831.

© 2025 The Author(s). Published by the Royal Society of Chemistry

Open Access Article. Published on 28 October 2025. Downloaded on 6/20/2026 5:31:48 PM. This article is licensed under a Creative Commons Attribution 3.0 Unported Licence.

21 T. Tarasova, A. A. Filatova and E. Y. Dolzhikova, Technical Problems and Perspectives of Implementing the Selective Laser Melting Method for Producing Structural Components for Aircraft, *Mater. Sci. Forum*, 2015, **834**, 29–33, DOI: 10.4028/www.scientific.net/msf.834.29.

22 N. Singh, P. Hameed, R. Ummethala, G. Manivasagam, K. G. Prashanth and J. Eckert, Selective laser manufacturing of Ti-based alloys and composites: impact of process parameters, application trends, and future prospects, *Mater. Today Adv.*, 2020, **8**, 100097, DOI: 10.1016/j.mtadv.2020.100097, ISSN 2590-0498.

23 P. Konda Gokuldoss, S. Kolla and J. Eckert, Additive manufacturing processes: Selective laser melting, electron beam melting, and binder jetting – selection guidelines, *Materials*, 2017, **10**, 672, DOI: 10.3390/ma10060672.

24 J. Baskaran, D. Muthukumaran, R. Shukla and P. Konda Gokuldoss, Manufacturability and deformation studies on a novel metallic lattice structure fabricated by selective laser melting, *Vacuum*, 2024, **222**, 113065, DOI: 10.1016/j.vacuum.2024.113065.

25 Z.-Q. Liu, R. Ma, G.-J. Xu, W.-B. Wang and Y.-H. Su, Effects of annealing on microstructure and mechanical properties of γ-TiAl alloy fabricated *via* laser melting deposition, *Trans. Nonferrous Met. Soc. China*, 2020, **30**(4), 917–927, DOI: 10.1016/S1003-6326(20)65265-7, ISSN 1003-6326.

26 H. Yue, H. Peng, R. Li, K. Qi, L. Zhang, J. Lin and Y. Su, Effect of heat treatment on the microstructure and anisotropy of tensile properties of TiAl alloy produced *via* selective electron beam melting, *Mater. Sci. Eng., A*, 2021, **803**, 140473, DOI: 10.1016/j.msea.2020.140473, ISSN 0921-5093.

27 M. S. Wang, E. W. Liu, Y. L. Du, T. T. Liu and W. H. Liao, Cracking mechanism and a novel strategy to eliminate cracks in TiAl alloy additively manufactured by selective laser melting, *Scr. Mater.*, 2021, **204**, 114151, DOI: 10.1016/j.scriptamat.2021.114151, ISSN 1359-6462.

28 D. Huang, Q. Tan, Y. Zhou, Y. Yin, F. Wang, T. Wu, X. Yang, Z. Fan, Y. Liu, J. Zhang, H. Huang, M. Yan and M.-X. Zhang, The significant impact of grain refiner on γ-TiAl intermetallic fabricated by laser-based additive manufacturing, *Addit. Manuf.*, 2021, **46**, 102172, DOI: 10.1016/j.addma.2021.102172, ISSN 2214-8604.

29 D. Wimler, J. Lindemann, M. Reith, A. Kirchner, M. Allen, W. G. Vargas, M. Franke, B. Klöden, T. Weißgärber, V. Güther, M. Schloffer, H. Clemens and S. Mayer, Designing advanced intermetallic titanium aluminide alloys for additive manufacturing, *Intermetallics*, 2021, **131**, 107109, DOI: 10.1016/j.intermet.2021.107109, ISSN 0966-9795.

30 L. Jiang, L. Lan, Ch Bai, H. Wang, S. Gao and B. He, Research progress on powder bed fusion additive manufacturing of TiAl-based alloy, *Int. J. Adv. Des. Manuf. Technol.*, 2024, **133**, 1045–1061, DOI: 10.1007/s00170-024-13843-x.

31 T. C. Dzogbewu and W. B. du Preez, Additive Manufacturing of Ti-Based Intermetallic Alloys: A Review and Conceptualization of a Next-Generation Machine, *Materials*, 2021, **14**(15), 4317, DOI: 10.3390/ma14154317.

32 C. Zhao, Z. Wang, D. Li, L. Kollo, Z. Luo, W. Zhang and K. G. Prashanth, Cu-Ni-Sn alloy fabricated by melt spinning and selective laser melting: a comparative study on the microstructure and formation kinetics, *J. Mater. Res. Technol.*, 2020, **9**(202), 13097–13105, DOI: 10.1016/j.jmrt.2020.09.047.

33 K. G. Prashanth and J. Eckert, Formation of metastable cellular microstructures in selective laser melted alloys, *J. Alloys Compd.*, 2017, **707**, 27–32, DOI: 10.1016/j.jallcom.2016.12.209.

34 J. J. S. Dilip, H. Miyanaji, A. Lassell, T. L. Starr and B. Stucker, A novel method to fabricate TiAl intermetallic alloy 3D parts using additive manufacturing, *Def. Technol.*, 2017, **13**(2), 72–76, DOI: 10.1016/j.dt.2016.08.001, ISSN 2214-9147.

35 I. Polozov, V. Sufiiarov, A. Kantyukov and A. Popovich, Selective Laser Melting of Ti_2AlNb-based intermetallic alloy using elemental powders: Effect of process parameters and post-treatment on microstructure, composition, and properties, *Intermetallics*, 2019, **112**, 106554, DOI: 10.1016/j.intermet.2019.106554, ISSN 0966-9795.

36 A. A. Nepapushev, D. O. Moskovskikh, K. V. Vorotilo and A. S. Rogachev, TiAl-Based Materials by *In Situ* Selective Laser Melting of Ti/Al Reactive Composites, *Metals*, 2020, **10**(11), 1505, DOI: 10.3390/met10111505.

37 Y. S. Kim, O. Gokcekaya, K. Sato, R. Ozasa, A. Matsugaki and T. Nakano, In-situ alloying of nonequiatomic TiNbMoTaW refractory bio-high entropy alloy *via* laser powder bed fusion: Achieving suppressed microsegregation and texture formation, *Mater. Des.*, 2025, **252**, 113824, DOI: 10.1016/j.matdes.2025.113824, ISSN 0264-1275.

38 A. Knaislová, P. Novák, J. Linhart, I. Szurman, K. Skotnicová, J. Juřica and T. Cegan, Structure and Properties of Cast Ti-Al-Si Alloys, *Materials*, 2021, **14**, 813, DOI: 10.3390/ma14040813.

39 A. Knaislová, P. Novák, M. Cabibbo, L. Jaworska and D. Vojtěch, Development of TiAl–Si Alloys – A Review, *Materials*, 2021, **14**(4), 1030, DOI: 10.3390/ma14041030.

40 F. H. Froes Fu-Sheng Sun, Effect of Mg on the microstructure and properties of TiAl alloys, *Mater. Sci. Eng., A*, 2003, **345**(1–2), 255–261, DOI: 10.1016/S0921-5093(02)00479-3, ISSN 0921-5093.

41 Q. Wang, R. Chen, Y. Yang, J. Guo, Y. Su, H. Ding and H. Fu, Effects of V and B, Y additions on the microstructure and creep behaviour of high-Nb TiAl alloys, *J. Alloys Compd.*, 2018, **747**, 640–647, DOI: 10.1016/j.jallcom.2018.03.055, ISSN 0925-8388.

42 K. G. Prashanth, S. Scudino, T. Maity, J. Das and J. Eckert, Is the energy density of a reliable parameter for materials synthesis by selective laser melting?, *Mater. Res. Lett.*, 2017, **5**, 386–390, DOI: 10.1080/21663831.2017.1299808.

43 C. Zhao, Z. Wang, D. Li, M. Xie, L. Kollo, Z. Luo, W. Zhang and K. G. Prashanth, Comparison of additively manufacturing samples fabricated from pre-alloyed and mechanically mixed powders, *J. Alloys Compd.*, 2020, **830**, 154603, DOI: 10.1016/j.jallcom.2020.154603.

44 H. Y. Jung, S. J. Choi, K. G. Prashanth, M. Stoica, S. Scudino, S. Yi, U. Kuehn, D. H. Kim, K. B. Kim and J. Eckert,

Open Access Article. Published on 28 October 2025. Downloaded on 6/20/2026 5:31:48 PM. This article is licensed under a Creative Commons Attribution 3.0 Unported Licence.

Fabrication of Fe-based bulk metallic glass by selective laser melting: A parameter study, *Mater. Des.*, 2015, **86**, 703–708, DOI: 10.1016/j.matdes.2015.07.145.

45 J.-S. Park, G. Yang and S.-W. Kim, A high tensile strength above 900 °C in β-solidified TiAl alloy through alloy design and microstructure optimization, *J. Alloys Compd.*, 2023, **947**, 169676, DOI: 10.1016/j.jallcom.2023.169676, ISSN 0925-8388.

46 Z. Li, C. Liao and Y. Liu, 700 °C Isothermal Section of the Al-Ti-Si Ternary Phase Diagram, *J. Phase Equilib. Diffus.*, 2014, **35**, 564–574, DOI: 10.1007/s11669-014-0325-7.

47 T. Maity, N. Chawke, J. T. Kim, J. Eckert and K. G. Prashanth, Anisotropy in local microstructure – Does it affect the tensile properties of the SLM samples, *Manuf. Lett.*, 2018, **15**, 33–37, DOI: 10.1016/j.mfglet.2018.02.012.

48 L. X. Xi, P. Ma, Y. D. Jia, A. K. Chaubey, Z. Wang and K. G. Prashanth, Influence of substrate plate heating on the fabrication of Al-12Si produced by selective laser melting, *Trans. Indian Natl. Acad. Eng.*, 2021, **6**, 1027–1036, DOI: 10.1007/s41403-021-00240-z.

49 K. G. Prashanth, S. Scudino and J. Eckert, Defining the tensile properties of Al-12Si parts produced by selective laser melting, *Acta Mater.*, 2017, **126**, 25–35, DOI: 10.1016/j.actamat.2016.12.044.

50 J. Lapin, M. Štamborská, T. Pelachová, T. Čegan and A. Volodarskaja, Hot deformation behaviour and microstructure evolution of TiAl-based alloy reinforced with carbide particles, *Intermetallics*, 2020, **127**, 106962, DOI: 10.1016/j.intermet.2020.106962, ISSN 0966-9795.

51 M. Fischer, D. Joguet, G. Robin, L. Peltier and P. Laheurte, *In situ* elaboration of a binary Ti–26Nb alloy by selective laser melting of elemental titanium and niobium mixed powders, *Mater. Sci. Eng., C*, 2016, **62**, 852–859, DOI: 10.1016/j.msec.2016.02.033, ISSN 0928-4931.

52 K. Li, X. Wang, H. Chen, X. Huang, G. Zhu and G. Tu, Fabrication of Ti_3Al-Based Intermetallic Alloy by Laser Powder Bed Fusion Using a Powder Mixture, *Materials*, 2023, **16**(7), 2699, DOI: 10.3390/ma16072699.

53 B. Zhang, J. Chen and Ch Coddet, Microstructure and Transformation Behavior of in-situ Shape Memory Alloys by Selective Laser Melting Ti–Ni Mixed Powder, *J. Mater. Sci. Technol.*, 2013, **29**(9), 863–867, DOI: 10.1016/j.jmst.2013.05.006, ISSN 1005-0302.

54 Q. Bizot, O. Politano, A. A. Nepapushev, S. G. Vadchenko, A. S. Rogachev and F. Baras, Reactivity of the Ti–Al system: Experimental study and molecular dynamics simulations, *J. Appl. Phys.*, 2020, **127**, 145304, DOI: 10.1063/5.0004550.

55 M. A. Buhairi, F. M. Foudzi and F. I. Jamhari, Review on volumetric energy density: influence on morphology and mechanical properties of Ti6Al4V manufactured *via* laser powder bed fusion, *Prog. Addit. Manuf*, 2023, **8**, 265–283, DOI: 10.1007/s40964-022-00328-0.

56 F. Huber, M. Rasch and M. Schmidt, Laser Powder Bed Fusion (PBF-LB/M) Process Strategies for In-Situ Alloy Formation with High-Melting Elements, *Metals*, 2021, **11**, 336, DOI: 10.3390/met11020336.

57 M. J. Matthews, G. Guss, S. A. Khairallah, A. M. Rubenchik, P. J. Depond and W. E. King, Denudation of metal powder layers in laser powder bed fusion processes, *Acta Mater.*, 2016, **114**, 33–42, DOI: 10.1016/j.actamat.2016.05.017, ISSN 1359-6454.

58 S. Lee, J. Kim and J. Choe, Understanding Crack Formation Mechanisms of Ti–48Al–2Cr–2Nb Single Tracks During Laser Powder Bed Fusion, *Met. Mater. Int.*, 2021, **27**, 78–91, DOI: 10.1007/s12540-020-00770-1.

59 S.-H. Park, O. Gokcekaya, M.-H. Oh and T. Nakano, Effects of hatch spacing on densification, microstructural and mechanical properties of β-solidifying γ-TiAl alloy fabricated by laser powder bed fusion, *Mater. Charact.*, 2024, **214**, 114077, DOI: 10.1016/j.matchar.2024.114077, ISSN 1044 5803.

60 L. Löber, F. P. Schimansky, U. Kühn, F. Pyczak and J. Eckert, Selective laser melting of a beta-solidifying TNM-B1 titanium aluminide alloy, *J. Mater. Process. Technol.*, 2014, **214**(9), 1852–1860, DOI: 10.1016/j.jmatprotec.2014.04.002, ISSN 0924-0136.

61 S. Peters, M. Perez and P. Blackwell, Integrating HIP and homogenisation heat treatment and its effect on the workability of a conventional peritectic TiAl alloy, *Intermetallics*, 2023, **158**, 107884, DOI: 10.1016/j.intermet.2023.107884, ISSN 0966-9795.

62 T. Klein, S. Niknafs, R. Dippenaar, H. Clemens and S. Mayer, Grain Growth and β to α Transformation Behavior of a β-Solidifying TiAl Alloy, *Adv. Eng. Mater.*, 2015, **17**(6), 786–790, DOI: 10.1002/adem.201400336.

63 M. Musi, B. Galy, A. Stark, N. Schell, M. Hantcherli, J.-P. Monchoux, A. Couret, H. Clemens and P. Spoerk-Erdely, How Si affects the microstructural evolution and phase transformations of intermetallic γ-TiAl based alloys, *Materialia*, 2022, **24**, 101475, DOI: 10.1016/j.mtla.2022.101475, ISSN 2589-1529.

64 Z. Kahrobaee and M. Palm, Experimental investigation of Ti–Al–Si phase equilibria at 800–1200 °C, *J. Alloys Compd.*, 2022, **924**, 166223, DOI: 10.1016/j.jallcom.2022.166223, ISSN 0925-8388.

65 S. Lee, M. S. Shin and Y. J. Kim, Development of Non-reactive Mold for Investment Casting of Ti-48Al-2Cr-2Nb Alloys, *Metall. Mater. Trans. B*, 2020, **51**, 861–869, DOI: 10.1007/s11663-020-01780-5.

66 G. Yang, X. Xu, Y. Liang, Y. Wang, G. Hao, Y. Zhai and J. Lin, Effects of Al and Mo on Microstructure and Hardness of As-Cast TNM TiAl Alloys, *Metals*, 2021, **11**(11), 1849, DOI: 10.3390/met11111849.

67 M. Schloffer, F. Iqbal, H. Gabrisch, E. Schwaighofer, F.-P. Schimansky, S. Mayer, A. Stark, T. Lippmann, M. Göken, F. Pyczak and H. Clemens, Microstructure development and hardness of a powder metallurgical multi phase γ-TiAl based alloy, *Intermetallics*, 2012, **22**, 231–240, DOI: 10.1016/j.intermet.2011.11.015, ISSN 0966-9795.

68 H. Z. Niu, Y. Y. Chen, S. L. Xiao and L. J. Xu, Microstructure evolution and mechanical properties of a novel beta γ-TiAl alloy, *Intermetallics*, 2012, **31**, 225–231, DOI: 10.1016/j.intermet.2012.07.012, ISSN 0966-9795.

© 2025 The Author(s). Published by the Royal Society of Chemistry

Open Access Article. Published on 28 October 2025. Downloaded on 6/20/2026 5:31:48 PM. This article is licensed under a Creative Commons Attribution 3.0 Unported Licence.

69 F. Perdrix, M.-F. Trichet, J.-L. Bonnentien, M. Cornet and J. Bigot, Relationships between interstitial content, microstructure and mechanical properties in fully lamellar Ti–48Al alloys, with special reference to carbon, *Intermetallics*, 2001, **9**(9), 807–815, DOI: **10.1016/S0966-9795(01)00066-8**, ISSN 0966-9795.

70 S.-J. Youn, Y.-K. Kim, S.-W. Kim and K.-A. Lee, Elevated temperature compressive deformation behaviors of γ-TiAl-based Ti–48Al–2Cr–2Nb alloy additively manufactured by electron beam melting, *Intermetallics*, 2020, **124**, 106859, DOI: **10.1016/j.intermet.2020.106859**, ISSN 0966-9795.

71 S.-J. Youn, Y.-K. Kim, H. S. Kim and K.-A. Lee, Improvement in the high temperature mechanical properties of additively manufactured Ti–48Al–2Cr–2Nb alloy using heat treatment, *Intermetallics*, 2023, **153**, 107784, DOI: **10.1016/j.intermet.2022.107784**, ISSN 0966-9795.

72 C. J. Boehlert, D. Hernández-Escobar, B. Ruiz-Palenzuela, I. Sabirov, J. Cornide and E. M. Ruiz-Navas, The effect of microstructure and strain rate on the 25 °C and 700 °C compression deformation behavior of powder metallurgy processed Ti–45Al–2Nb–2Mn (at%)-0.8 TiB2 (vol%) alloy, *Mater. Charact.*, 2021, **172**, 110856, DOI: **10.1016/j.matchar.2020.110856**, ISSN 1044-5803.

73 W. Li, M. Li, J. Liu, Y. Yang, S. Wen, Q. Wei, Ch Yan and Y. Shi, Microstructure control and compressive properties of selective laser melted Ti-43.5Al-6.5Nb-2Cr-0.5B alloy: Influence of reduced graphene oxide (RGO) reinforcement, *Mater. Sci. Eng., A*, 2019, **743**, 217–222, DOI: **10.1016/j.msea.2018.08.087**, ISSN 0921-5093.

74 W. Li, M. Li, Y. Yang, Q. Wei, D. Cai, J. Liu, Ch Yan and Y. Shi, Enhanced compressive strength and tailored microstructure of selective laser melted Ti-46.5Al-2.5Cr-2Nb-0.5Y alloy with different boron addition, *Mater. Sci. Eng., A*, 2018, **731**, 209–219, DOI: **10.1016/j.msea.2018.06.042**, ISSN 0921-5093.

75 M. Yan, F. Yang, H. Zhang, G. Yang, H. Zhang, Ch Zhang, M. Qi, J. Zhang, C. Chen and Z. Guo, Fine duplex Ti-48Al alloy with high strength produced by forging based on near-γ microstructure, *J. Alloys Compd.*, 2023, **942**, 169058, DOI: **10.1016/j.jallcom.2023.169058**, ISSN 0925-8388.

76 N. P. Lavery, J. Cherry, S. Mehmood, H. Davies, B. Girling, E. Sackett, S. G. R. Brown and J. Sienz, Effect of hot isostatic pressing on the elastic modulus and tensile properties of 316 L parts made by powder bed laser fusion, *Mater. Sci. Eng., A*, 2017, **693**, 186–213.

77 L. Hitzler, J. Hirsch, B. Heine, M. Merkel, W. Hall and A. Ochsner, On the anisotropic mechanical properties of selective laser-melted stainless steel, *Materials*, 2017, **10**, 1136.

78 J. Měsíček, T. Čegan, Q.-P. Ma, R. Halama, K. Skotnicová, J. Hajnyš, J. Juřica, P. Krpec and M. Pagáč, Effect of artificial aging on the strength, hardness, and residual stress of SLM AlSi10Mg parts prepared from the recycled powder, *Mater. Sci. Eng., A*, 2022, **855**, 143900, DOI: **10.1016/j.msea.2022.143900**, ISSN 0921-5093.

79 L. Chen, G. Yu, X. Zhang, L. Zhu, Y. Li and X. Ren, Effect of heat treatment on the microstructural evolution and mechanical property of nickel-based superalloy K447A manufactured by Powder Bed Fusion Laser Beam (PBF-LB), *Mater. Sci. Eng., A*, 2024, **910**, 146874, DOI: **10.1016/j.msea.2024.146874**, ISSN 0921-5093.

80 K. G. Prashanth, S. Scudino, H. J. Klauss, K. B. Surreddi, L. Loeber, Z. Wang, A. K. Chaubey, U. Kuehn and J. Eckert, Microstructure and mechanical properties of Al-12Si produced by selective laser melting: Effect of heat treatment, *Mater. Sci. Eng., A*, 2014, **590**, 153–160, DOI: **10.1016/j.msea.2013.10.023**.

81 S. Scudino, C. Unterfoerfer, K. G. Prashanth, H. Attar, N. Ellendt, V. Uhlenwinkel and J. Eckert, Additive manufacturing of Cu-10Sz bronze, *Mater. Lett.*, 2015, **156**, 202–204, DOI: **10.1016/j.matlet.2015.05.076**.